JACS
JOURNAL OF THE AMERICAN CHEMICAL SOCIETY
Article
pubs.acs.org/JACS

Ice Crystallization in Ultrafine Water−Salt Aerosols: Nucleation, Ice-Solution Equilibrium, and Internal Structure

Arpa Hudait and Valeria Molinero*

Department of Chemistry, The University of Utah, 315 South 1400 East, Salt Lake City, Utah 84112-0850, United States

ABSTRACT: Atmospheric aerosols have a strong influence on Earth's climate. Elucidating the physical state and internal structure of atmospheric aqueous aerosols is essential to predict their gas and water uptake, and the locus and rate of atmospherically important heterogeneous reactions. Ultrafine aerosols with sizes between 3 and 15 nm have been detected in large numbers in the troposphere and tropopause. Nanoscopic aerosols arising from bubble bursting of natural and artificial seawater have been identified in laboratory and field experiments. The internal structure and phase state of these aerosols, however, cannot yet be determined in experiments. Here we use molecular simulations to investigate the phase behavior and internal structure of liquid, vitrified, and crystallized water−salt ultrafine aerosols with radii from 2.5 to 9.5 nm and with up to 10% moles of ions. We find that both ice crystallization and vitrification of the nanodroplets lead to demixing of pure water from the solutions. Vitrification of aqueous nanodroplets yields nanodomains of pure low-density amorphous ice in coexistence with vitrified solute rich aqueous glass. The melting temperature of ice in the aerosols decreases monotonically with an increase of solute fraction and decrease of radius. The simulations reveal that nucleation of ice occurs homogeneously at the subsurface of the water−salt nanoparticles. Subsequent ice growth yields phase-segregated, internally mixed, aerosols with two phases in equilibrium: a concentrated water−salt amorphous mixture and a spherical cap-like ice nanophase. The surface of the crystallized aerosols is heterogeneous, with ice and solution exposed to the vapor. Free energy calculations indicate that as the concentration of salt in the particles, the advance of the crystallization, or the size of the particles increase, the stability of the spherical cap structure increases with respect to the alternative structure in which a core of ice is fully surrounded by solution. We predict that micrometer-sized particles and nanoparticles have the same equilibrium internal structure. The variation of liquid−vapor surface tension with solute concentration is a key factor in determining whether a solution-embedded ice core or vapor-exposed ice cap is the equilibrium structure of the aerosols. In agreement with experiments, we predict that the structure of mixed-phase HNO_3−water particles, representative of polar stratospheric clouds, consists of an ice core surrounded by freeze-concentrated solution. The results of this work are important to determine the phase state and internal structure of sea spray ultrafine aerosols and other mixed-phase particles under atmospherically relevant conditions.

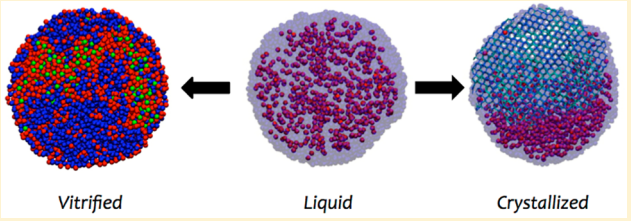

1. INTRODUCTION

Atmospheric aerosols influence cloud formation and growth and have significant impact on climate.[1,2] Sea spray aerosols (SSA) are a major component of the atmospheric particles in the marine boundary layer, the region of the troposphere directly above sea level.[3,4] The principal mechanism for the formation of sea spray aerosol is by bursting of bubbles from the sea surface microlayer.[5] Sea salts are the major component of sea spray aerosols, with an annual flux range estimated from 3000 to 5000 Tg yr^{-1}.[6] Alkali and alkaline earth cations (Na^+, Mg^{2+}, Ca^{2+}, and K^+) and anions (Cl^- and SO_4^{2-}) are the major ionic species present in SSA particles.[4,7−10] SSA modify their composition in the atmosphere by uptake of gas phase species such as SO_2, NO_x, and NH_3, a process known as chemical aging.[11] Heterogeneous chemical reactions on aerosol surfaces modify the distribution of trace atmospheric gases and subsequently alter the physical properties of the aerosols themselves. The phase state and corresponding morphology in aqueous aerosols are important in determining the rates and mechanisms of such heterogeneous reactions. Reaction of N_2O_5 with water leading to formation of HNO_3, for example, is slow in the gas phase[12] and is faster when the reaction occurs heterogeneously by adsorption over the ice surface, suggesting that the hydrolysis of N_2O_5 is heterogeneously catalyzed by the ice surface.[13] Accurate knowledge of the phase state (e.g., demixing, crystallization of ice or salt) and of the internal structure and the phases exposed to the surface of aqueous aerosols is essential to predict the mechanisms and rate of uptake of water, as well as the reaction of gas phase species like NO_3, N_2O_5, and HOBr, which lead to generation of halogen radicals responsible for polar ozone depletion.[10,14,15]

Experimental studies to understand the phase transitions and internal structures of aqueous aerosols in conditions relevant to the atmosphere have focused on millimeter- and micrometer-sized droplets.[10−12,14,16−20] Aerosol particles containing NH_4^+ and SO_4^{2-} ions are ubiquitous in the upper troposphere.[21] Considerable experimental effort has been made to study the

Received: April 2, 2014
Published: May 12, 2014

   dx.doi.org/10.1021/ja503311r | J. Am. Chem. Soc. 2014, 136, 8081−8093

phase behavior of micrometer sized $(NH_4)_2SO_4$—H_2O aerosols. These particles are formed by neutralization of H_2SO_4 with NH_3.[22] Differential scanning calorimetry (DSC) experiments by Bogdan and co-workers revealed the effect of droplet size on the mechanism of freezing in aqueous $(NH_4)_2SO_4$ droplets with salt content lower than the eutectic composition of 40 wt %.[23] Micrometer sized water droplets with subeutectic composition undergo homogeneous ice nucleation within the temperature range of about 210 to 225 K, while solute richer mixtures vitrify at around 172 K, resulting in a single freezing event, as observed in DSC thermograms.[24] Double freezing is observed in millimeter-sized droplets.[23] The second freezing event corresponds to crystallization of salt from the residual solution. Murray and co-workers used X-ray diffraction to show that for micrometer-sized droplets containing NH_4^+ and SO_4^{2-} ions, crystallization of the salt from the residual solution formed after homogeneous ice nucleation is strongly dependent on size of the droplet and solute concentration.[25] Crystallization of the residual solution is suppressed as the diameter of the droplet decreases from 10–20 μm to 2–5 μm. This is consistent with reports that in millimeter-sized droplets, ice crystallizes first, followed by crystallization of salt from the solute-enriched residual solution on further cooling.[23] Aqueous solutions of simple salts, such as LiCl, NaCl, and KCl also crystallize ice, vitrify, or crystallize a salt hydrate or pure salt with increasing solute content.[26,27] The tendency for salt to crystallize from the residual solution also decreases in the region around the eutectic, because nucleation and growth of crystals is hindered by the high viscosity of the solution. A DSC study of micrometer sized aqueous droplets containing NaCl also shows two freezing events corresponding to freezing of ice and ice and sodium chloride dihydrate ($NaCl\cdot 2H_2O$).[28] Optical microscopy images of crystallized aqueous microdroplets have been reported for H_2SO_4—H_2O and $(NH_4)_2SO_4$—H_2O aerosols.[29,30] These images indicate that freezing of these micrometer-scale drops results in an outer envelope of residual freeze-concentrated solution formed by the expulsion of solute molecules from water during the nucleation and growth of ice.[29,30] The study of the microscopic crystal nucleation processes that lead to ice formation within large volumes requires a nanoscopic resolution that cannot be attained with existing experimental methods. The same issue hinders the accurate determination of the phase state, internal structure and surface morphology of nanoscale aqueous aerosols. It is not known whether nanoscopic aerosols display the same internal structure and phase transformations of their micrometer and millimeter counterparts.

Ultrafine aerosols with sizes between 3 and 15 nm have been detected in large numbers in the troposphere and tropopause,[31,32] and the size of nascent aerosol nanoparticles has been recently tracked in field measurements.[33] Ultrafine aerosols arising from bubble bursting of natural and artificial seawater have been identified in laboratory and field experiments.[34−40] The characterization of the composition and internal structure of nanometer-sized aerosols, however, is still an extremely challenging task. Wyslouzil, Wilemski, and co-workers used a combination of small angle neutron scattering and modeling to unravel the internal structure of water–organic nanoparticles.[41,42] They found that the internal structure of water–butanol mixtures consists of a water-rich core covered by an organic shell,[41,42] while water–nonane mixtures have a "Russian doll" structure in which an almost spherical alkane core is partially wetted by the water phase.[43] Liquid aqueous nanodroplets involving carboxylic acids,[44,45] acetonitrile,[46] or ammonia[47] have been studied through molecular simulations and found to be demixed, although these solutes are fully miscible with water in bulk solutions. The structure of small water clusters, with less than ~250 molecules, containing alkyl cations, halide anions, sulfuric acid, and ammonia or amines has been investigated through modeling and experiments.[48−69] Nevertheless, the vitrification, crystallization, and internal structure of concentrated salt–water nanoparticles have not been studied to date through experiments or simulations. Freezing of pure water nanodroplets of radii in the range from 3 to 6 nm has been investigated through laboratory experiments[70−72] and molecular simulations.[73,74] The melting temperatures of water nanoparticles and ice nanocrystals have been determined with simulations[73,75] and thermodynamic modeling,[76] but not yet in experiments. To build beyond the state of the art, the present study aims to elucidate the effect of salts on the locus and temperature of ice nucleation, the temperature of ice–liquid equilibrium, and the internal structure of liquid, vitrified, and crystallized nanoscopic water–salt aerosols.

In this work, we investigate the structure, vitrification, nonequilibrium ice crystallization, and equilibrium ice melting temperatures of binary water–salt nanoparticles with radii from 2.5 to 9.5 nm and with up to 0.1 molar fraction of solute, using molecular dynamics simulations. We represent water with the monatomic water model mW[77] that accurately represents the structure of water in the liquid, glass, and ice states, as well as the thermodynamics and microscopic mechanisms of crystallization of water.[73,74,77−91] We consider a strongly hydrophilic solute that mimics LiCl ions,[88,92] and we demonstrate that the results should also be representative of the behavior of NaCl–water mixtures. The melting temperature of ice in the droplets depends on the droplet radius and composition of the solution. The global composition of the droplet and its size are insufficient to determine the ice-solution equilibrium temperature of the nanoparticles. We find that both vitrification and ice crystallization in the droplets lead to demixing of pure water from the solutions and result in significant changes to the internal structure of the particles. Vitrification of aqueous nanodroplets results in nanophase segregation into pure low-density amorphous ice (LDA) in coexistence with vitrified solute-rich aqueous glass, while ice crystallization in the nanoparticles leads to a spherical cap-like ice structure exposed to the vapor. The simulations reveal that nucleation of ice occurs at the solute-depleted subsurface of the water–salt nanoparticles.

2. MODEL AND METHODS

2.1. Model. Water is modeled with the monatomic water model mW, which represents each molecule as a single particle that interacts through anisotropic short-ranged potentials that favor "hydrogen-bonded" water structures.[77] The ions are represented by the coarse-grained solute S,[92] which presents strong attraction with water, but has no long-range (electrostatic) interactions and mimics LiCl ions in their effect on water structure, melting temperature of ice, and the crossover between crystallization and vitrification as a function of salt concentration.[88,92] The solute composition is reported in percentage moles,

$$X_S = \left(\frac{N_s}{N_w + N_s}\right)*100 \quad (1)$$

dx.doi.org/10.1021/ja503311r | J. Am. Chem. Soc. 2014, 136, 8081−8093

where N_S and N_W are the number of molecules of solute and water in the mixture, respectively. We distinguish between the global composition X_S^{global} of the particle, which encompasses all solute and water molecules in it, and the composition X_S of the liquid phase. The latter is the thermodynamic variable that controls the liquid-ice equilibrium in the binary particles.

2.2. Simulation Methods. We performed molecular dynamics simulation of binary water−salt nanodroplets using LAMMPS.[93] For simulations in the canonical (NVT) ensemble, the temperature was controlled with a Nose-Hoover thermostat with relaxation time 1 ps. The equations of motion were integrated using the velocity Verlet algorithm. The time step was 10 fs for the canonical simulations and 5 fs for the microcanonical (NVE) simulations to ensure energy conservation over long simulations.

2.3. Systems. We prepared spherical water droplets with N = 113 023, 13 824, 4235, and 2149 water molecules. The radius of each nanodroplet was calculated from the following:

$$R = \left(\frac{3vN}{4\pi}\right)^{1/3} \tag{2}$$

where v = 30.6 Å^3 is the molecular volume of ice in the mW model.[77] Nanodroplets with X_S^{global} = 5, 10 molar percent of solute systems were prepared by randomly replacing water by solute molecules. The radii of the aqueous nanoparticles in this study ranged from 9.4 to 2.5 nm.

2.4. Analysis. The *freezing temperature*, or temperature of maximum crystallization rate, T_f^{max}, was computed as the inflection[73] point in the fraction of ice versus temperature at the fastest cooling rate q_{max} that results in crystallization of the nanoparticle.[73,78,82] The nanoparticles were cooled at constant cooling rates of 1, 0.50, and 0.25 Kns^{-1}. Formation of ice along the simulation trajectories was identified using the order parameter q_6.[94] A cutoff of $q_6 > 0.55$ have been used to distinguish water molecules that belong to the ice phase. The *largest ice cluster* was defined as the largest cluster of connected neighboring water molecules that are identified as ice. The molecules were considered connected if they were within 3.5 Å, the first minimum in the radial distribution function of water. The radius of gyration of the largest ice crystallite, which quantifies its size and compactness, was computed as follows:

$$R_g^2 = \frac{1}{M}\sum_i m_i(r_i - r_{cm})^2 \tag{3}$$

where r_{cm} and M are the center of the mass and total mass of the largest ice cluster, respectively. The summation was made over all the atoms in the largest ice cluster. Cubic and hexagonal polymorphs of ice were identified using the CHILL algorithm.[82] The *four coordinated water molecules* were identified as those with four water neighbors within 0.35 nm.[81] The low-density amorphous ice (LDA) phase is identified by the domains of water molecules that are four-coordinated in the vitrified systems.

For each nanoparticle size and composition T_f^{max} is reported as an average over 5 independent cooling simulations at q_{max}. Additionally, independent isothermal simulations were performed to investigate the mechanism of ice nucleation and growth, in all cases at temperature $T > T_f^{max}$, for which nucleation is the limiting step in the crystallization. Each of these isothermal simulations were evolved for a maximum of 100 ns. Isoenergetic simulations in the microcanonical (NVE) ensemble were performed on the droplet with radius R = 4.7 nm with 5% and 10% global solute content. The initial energy of the system was obtained by equilibration of the droplets in canonical simulations for 0.5 ns at the selected initial temperatures, in the range from 160 to 200 K. Each system was evolved at constant energy for a maximum 50 ns, during which all droplets crystallized ice.

Freezing of the droplets at T_f^{max} results in the formation of multiple ice crystallites within each droplet. Heating of the crystallized droplets results in Ostwald ripening of these crystallites to form a single ice crystal. We started from the Ostwald ripened droplets with a single crystallite to generate configurations of the N-sized ice crystallite every 1 ns by isothermally evolving the systems for 5 ns, and then heating the configurations at 1 Kns^{-1}. In an equivalent manner, we took configurations at a temperature less than 2 K that of the final melting point and cool them at a rate of 1 Kns^{-1} to observe equilibrium cooling and verify that the process was reversible and a single equilibrium *melting temperature* $T_m(R, X_S)$ corresponded to the droplet of radius R in which a single ice crystallite coexisted with the solution with solute composition X_S.

The liquid−vapor *surface tension* γ_{LV} of the flat interface was determined for a range of solute compositions and two temperatures. Periodic liquid slabs with dimensions 3 × 3 × 10 nm^3 containing 1000 molecules and of the desired composition were created starting from the water slabs of refs 77 and 95 and randomly replacing water molecules by solute molecules. The surface tension was computed from the diagonal components of the pressure tensor tangential (p_T) and normal (p_N) to the liquid−vacuum interface using the following:[96]

$$\gamma_{LV}^{\infty} = \frac{L_z}{2}[\langle p_N\rangle - \langle p_T\rangle] \tag{4}$$

where ⟨...⟩ denotes an average over 50 ns of an NVT simulation.

The equilibrium *contact angle* θ of aqueous nanodroplets with 0, 5, 10, 15, and 20% solute on a planar ice surface were estimated at 275 K. Hemispherical droplets consisting of 5005 molecules and the desired composition were created and placed at the center of a polycrystalline ice slab of area 24 × 24 nm^2 and 1 nm depth prepared by crystallization of liquid water. The positions of the water molecules in the ice slab were kept fixed during the simulation to avoid melting (T_m of mW ice is 274 K[77]). The liquid droplets were equilibrated for 50 ns in an NVT simulation during which all the droplets underwent spreading over the ice surface to achieve an equilibrium conformation. The equilibrated droplets were evolved for further 10 ns in an NVT simulation and 5 configurations were selected from last 5 ns of the simulation, each at a difference of 1 ns. The contact angle was averaged over the set of equilibrium configurations collected for each of the five solute contents.

3. RESULTS AND DISCUSSION

3.1. Vitrification of Aqueous Nanoparticles Can Result in Demixing. Supercooled aqueous solutions either crystallize to form ice or vitrify into a nanosegregated or a homogeneous glass, depending on the rate of cooling, concentration of solutes, and size of the nanoparticles. Vitrification of bulk aqueous solutions with global solute content up to 20% results in domains of nanosegregated glass consisting of pure low-density amorphous ice (LDA) in coexistence with vitrified solute rich aqueous glass.[92] The coexistence of two distinct glasses in bulk vitrified solutions with less than 20% ions is supported by the existence of two glass transitions[98,99] and Raman spectra that are linear combinations of those of LDA and a concentrated water−solute glass.[100] Simulations with mW water and the S solute that mimics LiCl ions predict nanophase segregation of the glasses and a fraction of water in the LDA domains as a function of concentration in excellent agreement with the experiments.[92] The experiments and the simulations indicate that the fraction of water in the LDA phase is quite insensitive to the details of the water−solute interaction.[92,100] Vitrification of LiCl, NaCl, and KCl solutions produce essentially the same fraction of amorphous ice.[100] Moreover, the simulations indicate that the dimensions of phase segregation of the glass are about 5 nm. In the present work, we investigate the structure of the vitrified nanoparticles that have sizes comparable to those dimensions.

Phase segregation in the glass depends on the size of the nanodroplet. We fast cool liquid nanodroplets of radii 9.4, and 4.7 and 2.5 nm with 10% solute content at the lowest rate that results in vitrification of the particles in the simulations, 10 Kns^{-1}. The rates of crystallization of mW water around its

dx.doi.org/10.1021/ja503311r | J. Am. Chem. Soc. 2014, 136, 8081−8093

temperature of homogeneous ice nucleation are ~10^4 times faster than in experiments,[78,101] because of the higher diffusion coefficient of the monatomic model.[77] Hence, very high cooling rates are needed to bypass crystallization.[73,78,82] The extent of segregation decreases as the nanodroplet diameter approaches the characteristic dimensions of phase segregation, and also with the increase in solute content (Figure 1). The fraction of

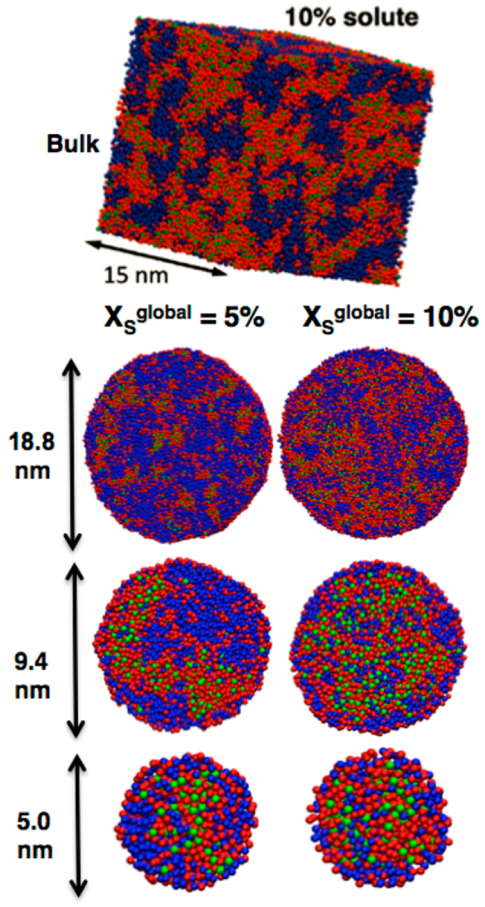

Figure 1. Vitrified aqueous mixtures in bulk and nanodroplets. Structure of bulk aqueous solution with 10% global solute content (top panel) and aqueous nanoparticles of different radii and global compositions 5% and 10% solute (lower panels) cooled at a rate of 10 Kns^{-1}. Nanodroplets are shown as a cut across their central plane, to display their interior. The number of water molecules in bulk aqueous solution and R = 9.4 nm aqueous nanoparticle is comparable, 110 592 and 113 023, respectively. In the vitrified mixtures, domains of pure low-density amorphous ice (blue balls, 4-coordinated water molecules) coexist and a glassy mixture of high-coordinated water (red balls) with ions (green balls).

water in the LDA phase in nanoparticles is lower than in the bulk system of same composition, and it decreases with the size of the droplet (Table 1). The four-coordinated liquid water domains that vitrify to LDA are the birthplace of ice,[88] therefore the extent of phase segregation impacts the rate of crystallization of ice in the nanoparticles. It is energetically favorable for hydrophilic solutes to be at the core of the vitrified droplet, where they can be fully hydrated,[102] rather than at the interface. Because of this, there is a lower effective solute concentration in the ~0.7 to 0.8 nm outer shell of the droplets. This particular property of hydrophilic solutes effectively

Table 1. Fraction of Water in the LDA Nanophase As a Function of the Solute Content (X_S^{global}) of the System in Bulk and Nanoparticles

X_S^{global} (% mole)	R (nm)	fraftion of LDA
5	bulk	0.67
5	9.4	0.61
5	4.7	0.58
5	2.5	0.50
10	bulk	0.44
10	9.4	0.37
10	4.7	0.32
10	2.5	0.28

controls the spatial occurrence of critical nuclei and growth of ice, which we elaborate on in Section 3.2.

3.2. Ice Crystallization in the Water–Salt Nanoparticles Starts at the Subsurface. Slow cooling of the nanoparticles results in the formation of ice. The ice crystallization temperature T_f^{max} and the maximum cooling rate that results in spontaneous ice crystallization in binary droplets, q_{max}, decrease with an increase in solute content for nanodroplets of a particular radius and also with a decrease in the size of the nanoparticle (Table 2). Experiments and

Table 2. Freezing Temperature and Critical Cooling Rate for Crystallization of Aqueous Nanodroplets

R (nm)	X_S^{global} (% mole)	T_f^{max} (K)	q_{max} (Kns^{-1})
4.7	0[a]	196 ± 2	1.0
4.7	5	182 ± 4	1.0
4.7	10	171 ± 2	0.5
3.1	0[a]	192 ± 3	1.0
3.1	5	173 ± 3	1.0
3.1	10	164 ± 2	0.25
2.5	0[a]	190 ± 3	0.5
2.5	5	174 ± 3	0.5
2.5	10	~152[b]	0.25

[a]From ref 73. Temperature of maximum crystallization rate (T_f^{max}) indicates the freezing temperature at the maximum cooling rate that results in spontaneous ice crystallization. [b]The N = 2149 (R = 2.5 nm) nanodroplet did not crystallize at the slowest rate of our study, q = 0.25 Kns^{-1}.

simulations indicate that the ice crystallization temperature of bulk water and its solutions is controlled by the water activity.[78,88,103−105] The S solute−mW water solutions of this study reproduce the concentration dependence of the ice crystallization temperature of bulk LiCl−water solutions.[88] NaCl is a less attractive solute than LiCl, and results in higher ice freezing temperatures in bulk mixtures.[106] It is therefore expected that the ice crystallization temperatures of NaCl−water nanoparticles will be higher than that for NaCl−water nanoparticles.

The temperature of maximum crystallization rate of ice,[47] T_f^{max}, coincides with the temperature at which supercooled liquid water experiences the maximum change in structure toward a four-coordinated liquid and a concomitant anomalous increase in the heat capacity and other response functions.[78] The locus of the structural transformation of the liquid, the thermodynamic anomalies, and T_f^{max} in mW water are about 25 K lower than those in experiment.[73,77,78,81] When corrected by that amount, the freezing temperatures of the water−salt nanoparticles of Table 2 (and the higher values expected for

dx.doi.org/10.1021/ja503311r | J. Am. Chem. Soc. 2014, 136, 8081−8093

NaCl–water particles) fall into the average temperatures of the upper troposphere.[107] Evaporative cooling of the nanodroplets,[47,108,109] and local fluctuations in atmospheric temperature, could result in homogeneous ice freezing of water–salt nanoparticles at lower altitudes.

The lines of glass transition and crystallization temperatures of the bulk mixtures cross at 20% solute for LiCl–water solutions in experiments[26] as well as for S–mW water solutions in simulations.[92] That crossing determines the maximum concentration of solutes that results in nucleation of ice from the mixtures. As the freezing temperatures vary slowly with size of the droplet (Table 2) and the glass transition temperatures of the droplet may be comparable to those of the bulk solution, we expect the limiting concentration for nanodroplets to be a slowly varying function of the radius, decreasing as the droplet size becomes smaller.

The trends for q_{max} in Table 2 signal that the maximum crystallization rate (i.e., the rate at the nose of the time–temperature transformation curve[78]) decreases with increasing confinement and solute content. This results from the smaller and scarcer four-coordinated liquid water domains in the smaller and more concentrated nanodroplets (Figure 1). The aqueous droplet with R = 2.5 nm and X_S^{global} = 10% did not undergo spontaneous ice crystallization at the slowest cooling rate of this study, 0.25 Kns^{-1}. Isothermal evolution of these droplets at 160 K, however, results in crystallization of ∼50% of the water molecules after 80 ns. This suggests that concentrated solutions of even smaller droplets can crystallize ice, although the probability to produce a fluctuation that results in a domain of pure water large enough to host a critical ice nucleus decreases sharply for small droplets.

In what follows, we investigate the locus of formation of the ice nuclei and the process of growth of ice crystallites in the aqueous nanoparticles. We monitor the appearance of ice nuclei in constant rate cooling simulations and the evolution of the nanoparticles through isothermal and isoenergetic simulations, and we analyze the extent to which ice nucleation and growth are affected by the distribution of ions and interfacial properties of the droplets. We also compare ice nucleation and growth in water–salt and pure water nanoparticles.

We first characterize the spatial solute distribution for aqueous liquid nanoparticles in the absence of ice. Figure 2 shows the radial density profile of the mole % of solute as a function of the distance from the center of the droplet. The core of the droplet has a homogeneous distribution of water and solute particles. The density of solute and water decrease on approaching the liquid–vapor interface; the density of solute falls faster than the density of water. This results in a radial density profile of solute concentration that starts dropping at 4 nm for the nanoparticle of radius 4.7 nm, indicating a depletion of solute in the 0.7 nm outer shell of the nanodroplet. Depletion of ions at the vapor/solution interface is characteristic of solutions of salts, including NaCl and other alkali halides, for which liquid–vapor surface tension increases with solute concentration.[102]

We find that critical ice nuclei exclusively appear at the subsurface of the nanodroplets, in the shell that is devoid of solutes. This is different from pure water nanoparticles, for which there is not a marked preference for nucleation at the subsurface the droplet.[73] Toxværd and co-workers investigated the crystallization of binary nanodroplets consisting of a Lennard–Jones mixture of strongly attractive solute and solvent and found that nucleation was initiated at the subsurface.[110]

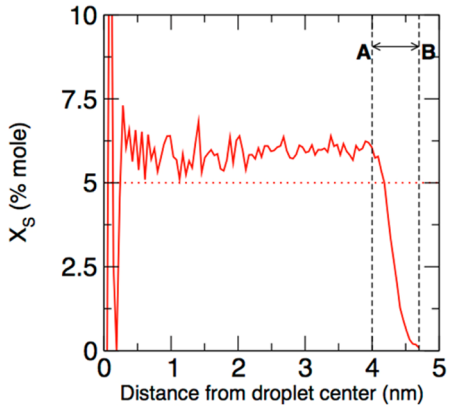

Figure 2. The outer shell of liquid droplets has lower ionic concentration than their core. Radial distribution of solute concentration in an R = 4.7 nm droplet with X_S^{global} = 5%. The region bound between the vertical black dotted lines marked by A and B represents the solute depleted outer droplet layer of width 0.7 nm. The width of the solute depleted region is the same for the droplet with X_S^{global} 5% and 10%. The critical ice nuclei form in the solute-depleted region.

They argued that to be a general result when the solute and the solvent form strongly attractive nonideal mixtures, which is the case for water–salt mixtures. Figure 3 illustrates the nucleation and growth of ice in nanodroplets at constant energy. After an induction period, ice nucleated in the subsurface of the particle and grew inward from the surface. Pure water domains with dimensions larger than the critical nuclei (∼2 nm diameter[78,88]) formed through the same concentration fluctuations that resulted in nanophase segregation of the vitrified mixtures.[92,111] These four-coordinated water domains are the birthplace of ice[78,88] and in aqueous nanodroplets form most easily in the outer shell of the particle, since the liquid–vapor interface is already depleted of solute. Crystallization of the nanoparticles in simulations at constant temperature or at constant cooling rate also starts at the subsurface but results in multiple ice crystallites within each particle. In next section, we discuss the internal structure of the crystallized water–salt droplets.

3.3. Ice in the Water–Salt Nanodroplets Forms a Spherical Cap Exposed to the Vapor. The ice crystallites that result from the isoenergetic crystallization of water–salt nanodroplets have the shape of a spherical cap exposed to the vapor (Figure 3). The crystallization of ice at constant energy heats the nanoparticle to the melting temperature of the ice crystallite in equilibrium with the resulting solution. When multiple crystallites nucleate close to the subsurface, these undergo Ostwald ripening within the nanoparticle,[73] consolidating into a more stable single crystallite as the nanoparticle heats up.

Crystallization of the water–salt nanoparticles at constant temperature or on cooling ramps also starts at the subsurface but produces multiple ice crystallites within each particle. Subsequent heating of these particles results in Ostwald ripening. The small crystallites have a lower melting temperature and dissolve to grow the largest crystallites, which also undergo extensive reorganization to become more compact, evidenced by a sharp decrease of their radii of gyration. The ripening results in the stable configuration for ice in water–salt nanodroplets: a spherical cap exposed to the particle surface. Figure 4 shows crystallized nanoparticles with two different sizes and global solute contents, but with the same

dx.doi.org/10.1021/ja503311r | J. Am. Chem. Soc. 2014, 136, 8081–8093

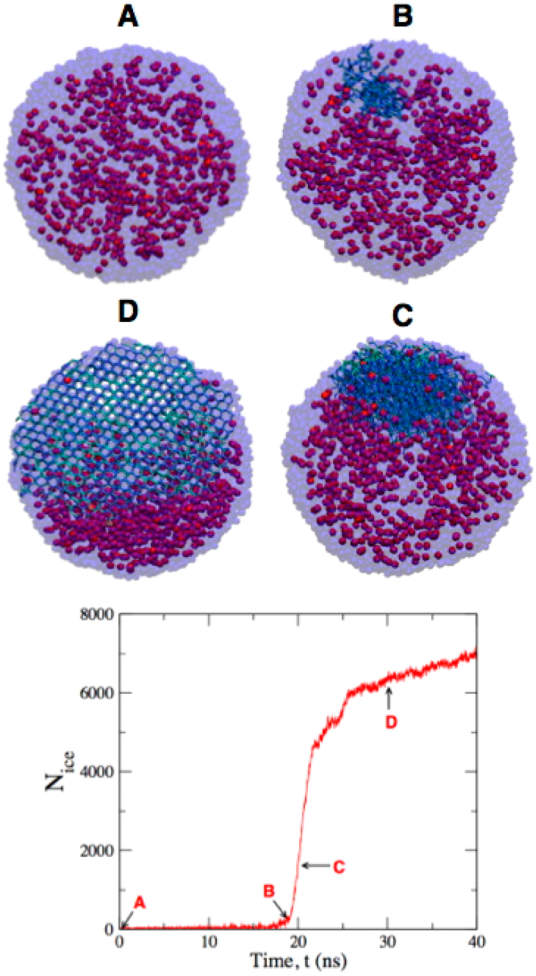

Figure 3. Isoenergetic crystallization of a water−salt nanoparticle. Aqueous nanoparticles in the atmosphere usually crystallize under constant energy conditions, because the growth of ice occurs in time scales that are significantly shorter than those required for the dissipation of the enthalpy of crystallization through thermal collisions with the surrounding gases or evaporation of water molecules. Panels A to D show snapshots of the nanodroplet with R = 4.7 nm and X_S^{global} = 5% at t = 0, 19, 20, and 30 ns, respectively. Solute particles are shown as solid red balls, and the transparent blue background corresponds to water in the liquid phase. Snapshot B displays the ice nucleation at the subsurface, while snapshot C shows the subsequent growth of ice. The lower panel shows the size of the ice crystallite (number of water molecules in the largest ice cluster, N_{ice}) as a function of the simulation time, points A to D correspond to the snapshots of the upper panels. The largest ice cluster is shown with cyan lines. The ice nucleus develops into a single ice crystallite. The particle was evolved microcanonically at the energy generated from pre-equilibration at 190 K (8 K above T_f^{max} of this droplet). As a result of crystallization, the temperature of the particle increased to 235 K.

concentration X_S of solute in the liquid phase. The ice formed in the nanodroplets is a stacking disordered ice I with cubic (C) and hexagonal (H) ice layers in a ratio of about 2C:1H. The formation of a stacking disordered ice with comparable fraction of cubic and hexagonal layers has been previously reported for the crystallization of bulk water and mixtures, and for pure water in nanopores and nanoparticles in simulations and in experiments for water in nanopores, bulk, and micrometer-sized droplets.[79,112−118] A hybrid structure with cubic and hexagonal ice layers was also inferred from the analysis of the diffraction

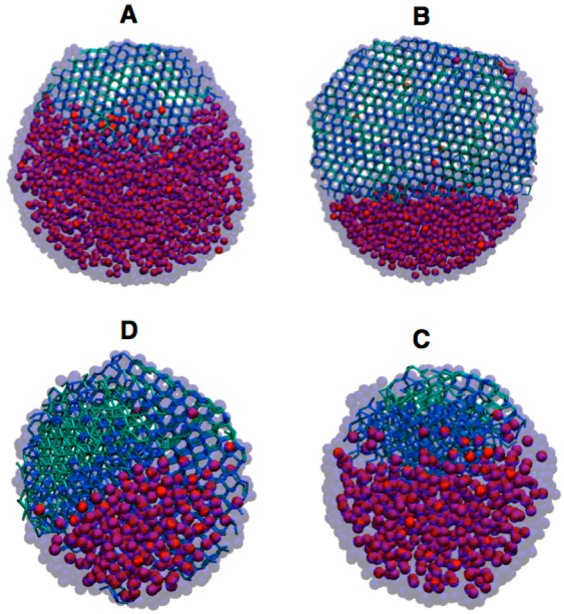

Figure 4. Crystallized nanodroplets in which ice is in equilibrium with solutions of composition X_S = 12.3%. Ice is shown as cyan lines connecting the water molecules, while liquid water is shown as transparent blue balls, and ions as solid red balls. B and D droplets have different radii (R) and N_{ice}, but they nevertheless have the same T_m and X_S, as shown in Figure 7.

patterns of crystallized bulk LiCl−water solutions in experiments.[119,120]

The shape and position of the ice crystallite in water−salt nanoparticles is unlike that found for pure water nanoparticles, for which the ice crystallite is spherical and centered at the core of the droplet, as shown in Figure 5. The ice crystallite wanders

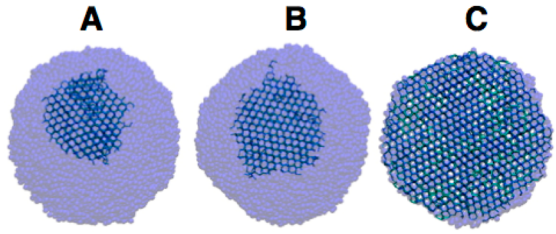

Figure 5. Structure and locus of ice in partially melted pure water nanodroplets. The snapshots show a droplet containing 13 824 water molecules at its melting point. The number of molecules in the ice phase (shown with sticks) are ∼1400, ∼2000, and ∼10000 for configurations A, B, and C, respectively. The blue shade shows the contour of the liquid phase. Each of these configurations is obtained from microcanonical simulations of the droplet with different total energies. The size of the ice crystallite in A is comparable to the one in binary nanodroplet C of Figure 4. C represents a fully crystallized water nanodroplet.

inside the pure water droplet but does not reach the liquid−vapor interface. We did not observe any instance in which the ice crystallite in the pure water particles relocates to the surface or reconstructs its geometry from sphere to spherical cap. It should be noted, however, that pure water particles in the atmosphere would most probably be found as all ice or all liquid, as there is a single temperature for which the two phases can coexist in a one component particle of a given size.

dx.doi.org/10.1021/ja503311r | J. Am. Chem. Soc. 2014, 136, 8081−8093

The difference in structure of the water−salt and pure water crystallized particles is also reflected in their mechanism of ice melting. During the melting of the water−salt particle, the ice crystallite remains exposed to the vapor while the melting of ice takes place at the ice−solution interface. Hence the melting of ice in the binary nanodroplets proceeds from the ice/solute interface in the interior of the droplet toward its surface. This is opposite to the melting of ice crystallite in pure water nanoparticles (Figure 5), where melting begins at the surface and proceeds to the center of the droplet increasing the width of the liquid layer covering the ice.[73]

The preference of the ice crystallites in the water−salt particles to be exposed to the vapor phase instead of being embedded in the solution phase or forming an outer shell reflects a subtle balance of the liquid−solid, solid−vapor, and liquid−vapor interfacial free energies. To understand the factors that determine the location of the ice crystallite, we estimated the reversible work (i.e., the free energy) to transform the exposed crystallite cap containing N_{ice} water molecules into a spherical crystallite with the same number of water molecules and centered at the core of the droplet:

$$G^{core} - G^{cap} = \gamma_{LS}(A_{LS}^{core} - A_{LS}^{cap}) - (\gamma_{SV} - \gamma_{LV})A_{SV}^{cap} \quad (5)$$

where G^{core} and G^{cap} represent the Gibbs free energy of ice crystallite in core and spherical cap and γ_{LS}, γ_{SV}, and γ_{LV} are the liquid−ice, ice−vapor, and liquid−vapor surface tensions, respectively. A_{LS}^{cap} and A_{SV}^{cap} represent the liquid−ice and ice−vapor surface area of the spherical cap conformation, while A_{LS}^{core} represents the liquid−ice surface of the core ice. Using Young's equation,

$$\gamma_{SV} - \gamma_{LV} = \gamma_{LV}(\cos\theta - 1) + \gamma_{LS} \quad (6)$$

where θ is the contact angle between a droplet of liquid solution and ice, and substituting eq 6 in eq 5, yields the following expression for the free energy difference for core and cap conformations,

$$G^{core} - G^{cap} = \gamma_{LS}(A_{LS}^{core} - A_{LS}^{cap}) - \{\gamma_{LV}(\cos\theta - 1) + \gamma_{LS}\}A_{SV}^{cap} \quad (7)$$

A high value of γ_{LV} favors cap over core, because a particle with the cap configuration has lower liquid−vapor area than that in the core configuration.

We use eq 7 to estimate $G^{core} - G^{cap}$ as a function of the fraction of crystallized water in aqueous nanodroplets of various compositions and determine which is the stable configuration. We calculate analytically the areas involved in eq 7 using the appropriate geometrical relations for a sphere and a spherical cap. In what follows, we first discuss the values of γ_{LS} from literature data for mW water and experimental aqueous solutions, and determine γ_{LV} and θ as a function of concentration from simulations with flat surfaces. We then elaborate the factors that need to be considered for accurate determination of surface tensions, γ_{LV} and γ_{LS} of the droplets and discuss the evolution of the sign of $G^{core} - G^{cap}$ as a function of global composition, size, and fraction of crystallized water in the nanodroplets. We close this section with an analysis of whether the structures predicted for S−mW (a model for LiCl−water) particles hold for i) aqueous droplets with NaCl, which is the more abundant salt in sea spray aerosols, ii) for water−HNO_3 solutions, which are important in polar stratospheric clouds, and iii) less hydrophilic solutes.

The surface tensions depend, in principle, on temperature, solute concentration and curvature of the surface. We computed the *surface tension of the flat liquid−vapor surface*, γ_{LV}^{∞} for bulk mW−S mixtures at two temperatures, 220 and 293 K, and compared the results to experimental liquid−vapor surface tension for water−LiCl mixtures at 293 K (Figure 6).

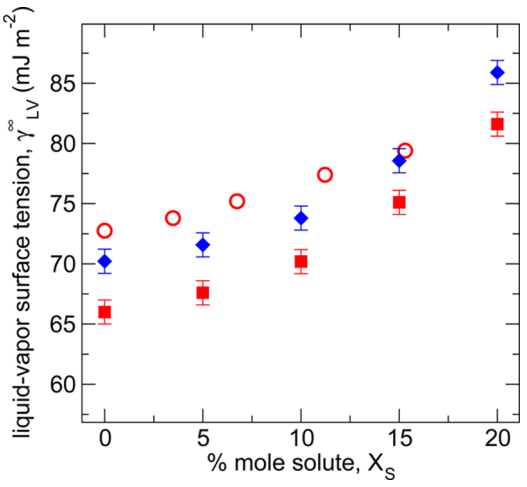

Figure 6. Liquid−vapor surface tension of a flat interface as a function of solute concentration. The blue diamonds correspond to simulations at 220 K (close to the melting temperatures in the droplets), the red squares to simulations at 293 K, and the red circles of experiments of LiCl−water solutions at 293 K from ref 121.

γ_{LV}^{∞} of the mW−S mixtures increases with solute concentration and on cooling in good agreement with experimental results for water−LiCl solutions.[121] The increase in γ_{LV}^{∞} with solute concentration is consistent with a continuous enrichment of ions in the solute-depleted shell of the liquid−vapor interface. Sun and co-workers used atomistic simulations to study the curvature dependence of γ_{LV} for pure water and water−salt droplets as a polynomial function of the inverse of the equimolar radius.[122] Their fitting suggests a nonmonotonous $\gamma_{LV}(R)$ that reaches maximum value ~33% higher than γ_{LV}^{∞} at R = 3.2 nm. The curvature dependence of γ_{LV} is usually described by the Tolman equation, $\gamma_{LV}(R) = \gamma_{LV}^{\infty}/(1 + 2\delta/R)$,[123−126] although a comparison of surface tensions predicted with that equation and with exact thermodynamic relations indicates that Tolman's equation should not be valid for nanodroplets.[127] To estimate $G^{core} - G^{cap}$ with eq 7, we approximated the liquid−vapor surface tension of the droplet with the one of the planar surface, γ_{LV}^{∞} calculated at 220 K multiplied by the ratio of $\gamma_{LV}(R)/\gamma_{LV}^{\infty}$ obtained for the water−salt droplets of ref 122. We have also taken into account the concentration dependence of γ_{LV}^{∞} since the solution becomes more concentrated during ice crystallization and growth.

The experimental *liquid−ice surface tension* γ_{LS} of solutions of salts was determined by Hardy and Coriell from the growth of cylindrical ice crystals from supercooled solutions; they concluded that γ_{LS} increases with addition of salts, from 25 mJm^{-2} for pure water to 30 mJm^{-2} for 0.1 M NaCl.[128] It should be noted, however, that the surface tension of pure water in that study was underestimated compared to the accepted value in the literature, 32 to 33 mJm^{-2}.[129,130] Rasmussen and MacKenzie estimated the ice−liquid surface tension of mixtures of water with various solutes (none of them salts) from the ice nucleation rates interpreted within the framework of classical

dx.doi.org/10.1021/ja503311r | J. Am. Chem. Soc. 2014, 136, 8081−8093

nucleation theory.[131] Different from the other study, they concluded that γ_{LS} decreases with increasing solute content. However, as nucleation occurs at lower temperatures for concentrated solutions, it is not straightforward to separate from that analysis the effect of temperature and concentration in γ_{LS}. The curvature dependence of the ice−liquid surface tension was investigated by Bogdan through the calculation of Gibbs adsorption at the equimolar dividing surface.[132] He estimated that, as the dimensions of the ice crystallites approach the nanometer scale, the ice-solution surface tension displays significantly higher curvature dependence than the ice-vapor surface tension. More importantly, his analysis indicates that the Tolman length δ for the liquid−ice interface increases significantly on supercooling. The latter is consistent with the continuous structural transformation of deeply supercooled water into a four-coordinated liquid, accompanied by a sharp decrease in the excess thermodynamic functions between liquid water and ice.[78] These considerations suggest that corrections to the liquid−ice surface tension of a flat surface γ_{LS}^{∞} may be non negligible for the crystallites in the smallest droplets of Figures 4. The liquid−ice surface tension for mW water was calculated by Limmer and Chandler at the melting temperatures of ice confined in cylindrical pores.[86] They found γ_{LS} to decrease from 35.3 mJm^{-2} at 273 K to 22.9 mJm^{-2} at 200 K. These calculations integrated over all crystallographic faces of ice in a cylindrical geometry radii, hence they account for the curvature dependence of γ_{LS}. Ice−liquid surface tensions of aqueous solutions could only be determined indirectly in experiments and have never been computed from molecular simulations. We do not attempt such a calculation in the present study. On the basis of the little experimental dependence on γ_{LS} with salt content,[128] we adopt the temperature and radii dependent values of γ_{LS} for pure mW ice/liquid from ref 86 for the calculation of $G^{core} - G^{cap}$ of the aqueous nanoparticles.

The contact angle θ of a pure, macroscopic water droplet on ice at the vicinity of its freezing point (273 K), has been estimated to be 12 ± 1°, the value of its receding contact angle.[133] We determined the equilibrium contact angle of water nanodroplets with a range of solute content from 0% to 20% over a planar ice surface at 275 K, keeping the ice slab fixed to prevent its melting. The contact angle for the pure water droplet on ice was found to be 24 ± 3°. Since the equilibrium contact angle is always greater than the minimum receding contact angle, the equilibrium θ is expectedly greater than the experimentally calculated minimum receding contact angle of 12°. We find that the contact angle of the nanodroplets on ice increases with the salt concentration, approximately by 1° every 1% increase in X_S. We neglect the temperature dependence of the contact angle and use the $\theta(X_S)$ determined from the simulations to account for the increasing concentration in the solution with the growth of the ice crystallite within each droplet in the calculation of $G^{core} - G^{cap}$.

With the γ_{LV}, γ_{LS}, and θ discussed above, and the analytical areas calculated for the cap and core configurations, we used eq 7 to compute $G^{core} - G^{cap}$ as a function of (i) initial solute content X_S^{global}, (ii) advance of the crystallization (which, along with X_S^{global}, determines the actual X_S), and (iii) radius R of the droplet. Our calculations indicate that the larger the size of the droplet and the higher the concentration of the solution in equilibrium with ice, the more stable is the cap configuration compared with the core one. For example, on crystallizing ice from a droplet with R = 4.7 nm and X_S^{global} = 5%, the transition from core to cap is predicted to occur when 8.1% of the water has crystallized (the ice crystallite contains ∼1000 water molecules), at which point X_S of the solution in coexistence with ice is 5.72%. We recall that for X_S^{global} = 5% with R = 4.7 nm particle, spontaneous ice crystallization at T_f^{max} = 182 ± 4 K results in crystallization of about 50% of the water. Under those conditions, we estimate that, per mole of droplets, $G^{core\ is}$ 1671 kJ above G^{cap}. For a smaller, R = 3.1 nm, droplet with same global concentration (X_S^{global} = 5%) and advance of crystallization (50%), $G^{core} - G^{cap}$ decreases to 803 kJ per mol of droplets. For micrometer-sized droplets with X_S^{global} = 5%, we predict that the cap conformation becomes more stable than the core already when 38% of water has crystallized. The thermodynamic stability of the spherical cap conformation of ice relative to the spherical core conformation with the advance of crystallization or global solute content explains the outcome of our simulations in which we exclusively observe core ice for pure water droplets and spherical cap ice configurations for the water−salt nanoparticles.

A sensitivity analysis of the variables that determine $G^{core} - G^{cap}$ indicates that the slope of the liquid−vapor surface tension with solute concentration is the most important property for determining whether cap or core is the favored conformation of the crystallized particle. If γ_{LV} increases with concentration, as is the case for the alkali halides,[102] then the more the crystallization advances, the higher the penalty for having an extended liquid−vapor interface, favoring the formation of an ice cap. Reasonable variation of the contact angle and the liquid−ice surface tension do not affect this result; it only changes −slightly- the concentration (or advance of crystallization) at which cap becomes more stable than core. NaCl is the major salt component in sea spray aerosol, and the γ_{LV} of its aqueous solutions increases with concentration with a slope almost indistinguishable from that of LiCl.[102] We predict that crystallized NaCl−water particles will favor the cap conformation, exposing ice to the vapor.

Laboratory experiments on micrometer-sized nitric acid-rich HNO_3—H_2SO_4—H_2O droplets, which are surrogates for polar stratospheric cloud particles, indicate that the ice in the crystallized particles is covered by a freeze concentrated solution.[30,134] Different from the alkali halides, the liquid−vapor surface tension of HNO_3 strongly decreases with concentration.[102,135] γ_{LV} of H_2SO_4 solutions is non-monotonous with concentration, increasing slightly up to concentrations of about 50% weight and precipitously decreasing for more concentrated solutions. The global concentration of the acids in the droplets of ref 30 is 23% wt HNO_3 and 0 to 6 wt % H_2SO_4. The eutectic solution in equilibrium with ice is 32 wt % (about 11% mole) of acid.[30] Using γ_{LV} of HNO_3 solutions of ref 102 and γ_{LS} are the same as in the S−mW solutions, we evaluated $G^{core} - G^{cap}$ for water−HNO_3 particles with a global concentration of 5% mole of HNO_3 for which 50% of the water has crystallized, resulting in a solution with ∼10% of HNO_3 in equilibrium with ice. In agreement with the laboratory experiments, we predict the ice core configuration to be the most stable state for micrometer-sized particles. We also find that the core configuration is the most stable one for crystallized water−HNO_3 nanoparticles, not yet measured in experiments. We conclude that the change in liquid−vapor surface tension with concentration is a key parameter for the prediction of the internal structure of crystallized atmospheric particles of all sizes.

The solutes considered above are highly hydrophilic. We now briefly assess the effect of reducing water−solute attractive interactions on the internal structure of crystallized aqueous nanoparticles. We performed simulations of binary droplets of radius R = 4.7 nm and with strength of interactions between water and solute, $\epsilon_{water-solute}$ = 3, 4, and 5 kcal mol^{-1}, all less than the 6.189 kcal mol^{-1} for water with solute S that mimics LiCl. We find that solutes with enthalpy of hydration lower than the enthalpy of vaporization of water behave as if they were hydrophobic, resulting in phase segregation in the liquid nanodroplets. Enthalpies of hydration were calculated from the difference in enthalpy of a cluster containing 417 water molecules and the same cluster equilibrated with a solute particle.[136] Nanodroplets of the weaker solutes display a distinctly different spatial solute distribution from the very hydrophilic, ionic mixtures discussed above. Aqueous nanodroplets for which the strength of the water−solute interaction potential is $\epsilon_{water-solute} \leq 4$ kcal mol^{-1} undergo phase segregation to form solute clusters in the liquid state already at temperatures as high as 298 K. Ice crystallization in these hydrophobic solute−water nanodroplets results in an ice crystallite exposed to vapor phase, as it occurs to the salt solutions, however the shape of the ice crystallite is not a spherical cap. The structure of the ice crystallite in hydrophobic solute−water nanodroplets is often distorted as the ice nucleate and grows in the pure water domains confined between clusters of segregated solute. The weakening of water−solute interactions adds a new complexity, phase segregation already within the high temperature liquid, which must be considered in the prediction of internal structure of binary nanoparticles in the liquid, glass and crystallized states.

3.4. Global Concentration and Size of Droplet Are Not Sufficient to Determine the Melting Temperature of Ice in Binary Nanoparticles. In this final section, we compute the equilibrium melting temperatures T_m of water−salt nanoparticles containing a single ice crystallite as a function of particle radius and composition. The ice crystallite in Ostwald ripened droplets is in thermodynamic equilibrium with the solution, making the evolution of the system along the melting curves reversible with respect to changes in temperature. This allows for the determination of $T_m(R, X_S)$ for a wide and continuous range of compositions for each particle. Figure 7 shows the equilibrium melting line $T_m(X_S)$ of the bulk solution (blue line) and the melting lines of nanoparticles $T_m(R, X_S)$ of two different sizes (R = 4.7 nm in red and R = 3.1 nm in green) and two global compositions (X_S^{global} = 5% with solid lines and 10% with dashed lines). The equilibrium melting temperature of binary nanoparticles depends on the radius of the nanoparticle, the size of the ice crystallite and the composition of the solution. Knowledge of the global composition and radius of a particle is insufficient to predict its melting temperature: each (R, X_S^{global}) particle has a *range* of melting temperatures that depends on the composition X_S of the solution in equilibrium with the ice crystallite or, equivalently, on the fraction of water crystallized. Nanoparticles with identical ice melting temperatures and solution composition X_S, such as those represented by B and D in Figure 7, can have quite different sizes and fraction of ice, as shown in Figure 4. The melting temperature of the nanoparticles has a steeper dependence with solute concentration than the bulk solution.

The solute and water models used in this work represent quite accurately the thermodynamics of the ice−water

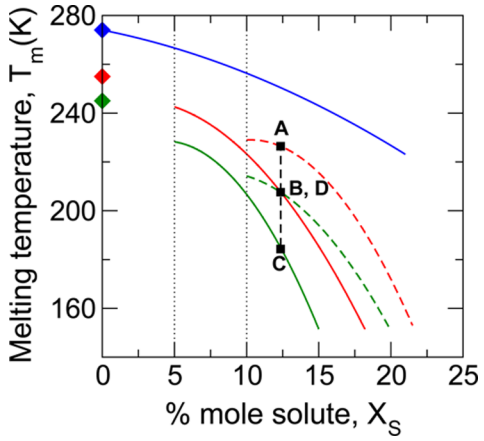

Figure 7. Melting temperature of ice as a function of solute content X_S in binary water−salt mixtures. Each curve corresponds to a different system. The blue line represents the melting temperature of the bulk solution, from ref 88. The four other lines correspond to nanoparticles with radii R = 4.7 nm (red lines) and R = 3.1 nm (green lines). For each of these nanoparticle sizes, we show the melting lines as a function of solute content X_S in equilibrium with the ice crystallite for two distinct global concentrations of solute X_s^{global} = 5% (solid lines) and 10% (dashed lines). Note that the lower X_S (when all ice just melted) is equal to X_s^{global}. The diamond symbols in the X_S = 0 axis indicate the melting temperatures of pure water in bulk (blue diamond, T_m = 274 K) and in nanoparticles of R = 4.7 nm (red diamond, T_m = 255 K) and R = 3.1 nm (green diamond, T_m = 245 K). The A−D state points correspond to the four systems shown in Figure 4. States B and D have same T_m and X_S but different fraction of water crystallized and droplet size, illustrating that the equilibrium melting temperature results from an interplay of three variables: X_S or N_{ice}, X_S^{global}, and R.

equilibrium in bulk water, in pure water nanoparticles, and bulk LiCl−water.[77,88,136] While still a very hydrophilic solute, Na^+ interaction with water is not as strong as the one of Li^+,[137] and NaCl produces a less dramatic decrease of the melting point of bulk solutions than LiCl.[138,139] The effect of these two salts on the surface tension of water, however, are almost identical.[102] On the basis of these differences, we expect that the melting temperatures of sea spray NaCl−water ultrafine aerosols will be higher than those reported here for LiCl−water particles, have a less steep dependence with concentration but a similar dependence with size. Accurate prediction of the phase diagram for other salts, however, requires the derivation of an exact relationship for $T_m(R, X_S)$ from thermodynamic data. For pure water droplets, the melting temperature depends only on the radius of the particle (diamond symbols in Figure 7) and is accurately represented by the Gibbs−Thomson equation, $T_m(R) = T_m^{bulk} - K_{GT}/(R - d)$, where the Gibbs−Thomson constant K_{GT} = 82 ± 5 Knm and the width of the premelted layer covering the ice crystallite is d = 0.26 ± 0.05 nm.[73] The Gibbs−Thomson equation is derived within the capillarity approximation. The derivation of an equivalent relation to describe the equilibrium $T_m(R, X_S)$ of ice and solution within the binary droplets is quite nontrivial because of the complexity introduced by the dependence of the surface tensions with T, surface curvature, and X_S (see section 3.3), and the nonideality of the mixture. It should be noted that the curvature dependence of the surface tension invalidates the capillarity model of classical nucleation theory, which assumes that the surface tension of a nanodroplet is the same as that of the macroscopic planar surface tension.[140] Němec and co-workers

dx.doi.org/10.1021/ja503311r | J. Am. Chem. Soc. 2014, 136, 8081−8093

derived the work of formation for a homogeneous liquid water−NaCl nanodroplet from the binary vapor under the assumption that the surface tensions were independent of curvature.[141] To our knowledge, there has been no treatment of the thermodynamics of coexistence of a crystal and a solution within a nanoscopic droplet. We refer the reader to the comprehensive article of Reguera and Reiss for a discussion of the subtleties involved in the choice of thermodynamic models and approximations for a simpler case, the equilibrium of a binary vapor and an ideal one-phase liquid droplet.[140]

4. CONCLUSIONS

We investigated the internal structure, ice−liquid equilibrium, nonequilibrium crystallization, locus of ice nucleation, and conditions for vitrification of aqueous binary salt−water nanoparticles with up to 20% moles of ions and radii ranging from about 2.5 to 9.4 nm. The simulations of this work were performed with mW water and the solute S that mimics LiCl ions. Our analysis indicates that NaCl−water nanoparticles would present the same structures in the liquid, glass, and crystallized state as well as same locus of ice nucleation than LiCl−water nanoparticles. To our knowledge, this is the first study of ice crystallization and internal structure of glass and crystallized water−salt nanoparticles, a model system for ultrafine sea spray aerosols.

The elucidation of the internal structure of liquid, vitrified, and crystallized water−salt nanodroplets is a central result of this work. We find that while water and salt in the liquid droplets are fully mixed, the 0.8 nm outer shell of the droplets is depleted of ions, exposing a water-enriched interface to incoming atmospheric molecules. The simulations reveal that the water-rich outer layer is the locus of nucleation of ice in these ultrafine aerosols. Crystallization and vitrification of the water−salt nanoparticles result in internally mixed aerosols containing a pure water phase and a concentrated water−salt amorphous phase. The water nanophase in the vitrified aerosols is low-density amorphous ice in the form of nanoscopic domains that occur through all the droplet volume. The water nanophase that results from crystallization of particles is stacking disordered ice I with short stacks of layers of cubic and hexagonal ice.

The ice nanophase in water−salt particles has the form of a spherical cap exposed to the surface of the aerosol and in equilibrium with a freeze-concentrated water−salt solution. The internal structure of the water−salt ultrafine aerosols is different from the one of partially crystallized pure water nanoparticles, which consists of a spherical ice core surrounded by liquid. We estimated the free energy difference between cap and core conformations for the binary aerosols as a function of global solute content, fraction of water crystallized, and the size of the particles. We found that the thermodynamic stability of the cap increases with these three variables: we predict that, except for very dilute solutions of small nanoparticles, the internal structures of the thermodynamically stable state of crystallized water−salt ultrafine aerosols expose both ice and a concentrated amorphous mixture on their surfaces. We predict that the equilibrium internal structure of concentrated micrometer-sized water−salt droplets is the same as for the corresponding nanodroplets: an internally mixed aerosol with a spherical ice cap in contact with a concentrated water−salt solution. The presence and extent of these distinct surfaces should have important consequences for the molecular uptake and chemical reactivity of crystallized water−salt aerosols.

Not all crystallized atmospheric particles expose ice on their surfaces. We find that the change of the liquid−vapor surface tension with increasing solute content is a defining characteristic to determine whether a crystallized particle will form a solution-embedded ice core or a vapor-exposed ice cap. Optical microscope studies of micrometer-sized droplets of HNO_3—H_2SO_4—H_2O crystallized at the slow cooling rates and rewarmed to temperatures just below their melting, show ice crystallites surrounded by a residual freeze-concentrated solution.[30] The internal structure of these particles and whether they expose ice on their surfaces has been the subject of a recent debate.[29,116,142] Our estimation of the free energy of core and cap conformations in crystallized HNO_3—H_2O particles indicates that—in agreement with the results by Bogdan et al.[29,30]—an ice core surrounded by solution is the equilibrium internal structure of these micrometer-sized particles. We predict the same internal structure for crystallized nitric-acid rich water nanoparticles.

Our analysis points to the importance of determining the temperature variation of γ_{LV} of atmospherically relevant solutions for predicting the equilibrium internal structure of crystallized aerosols. Equilibration of the internal structure, however, may be more difficult to achieve in large aerosol particles than in nanoparticles. Therefore, care should be taken on extrapolating the equilibrium predictions to micrometer-sized aerosols formed under nonequilibrium conditions. The thermal history of the particles—whether they heated up on crystallization, their temperature was controlled by a thermal bath made of gases or other particles, or they were subjected to cycles of cooling and warming—should be taken into account when assessing whether the internal structure of large particles is in equilibrium.

The global composition and the radius are insufficient to unequivocally determine the thermodynamic state of binary droplets. The equilibrium melting temperatures of ice in the binary nanoparticles depend on the size of the droplet and the composition of the solution in equilibrium with the crystallite. Alternatively, the radius of the particle, the fraction of water in the ice phase and the global droplet composition may be used as variables. The equilibrium melting $T_m(R,X_S)$ and nonequilibrium freezing temperatures $T_f(R,X_S)$ computed in this work provide a framework for predicting the state of water and internal structure of atmospheric aqueous nanoparticles. The equilibrium melting temperatures decrease monotonically with the decrease of radius of the nanoparticle and increase of solute. Prediction of the melting temperature of the binary droplets requires accurate knowledge of the activity coefficients of water in the mixtures, as well as surface tension of the liquid−vapor, liquid−solid, and solid−vapor and the dependence of these quantities with concentration and droplet size. Accurate determination of these parameters is of fundamental importance to predict the internal structure and phase state of atmospheric nanoparticles.

Definitive knowledge of the phase state, internal structure, and surface morphology of aqueous particles at conditions relevant in the atmosphere is essential to determine uptake coefficients and the rate of atmospherically relevant heterogeneous reactions.[143−146] While the present study was focused on water−salt binary systems, a variety of organic molecules can be found in sea spray aerosols. The extent by which organic molecules modulate the internal structure of aqueous solutions of salts in the liquid, vitreous, and crystallized states, and whether organic molecules affect the locus and mechanisms of

ice nucleation, are important issues that will be addressed in future work.

AUTHOR INFORMATION

Corresponding Author

Valeria.Molinero@utah.edu

Notes

The authors declare no competing financial interest.

ACKNOWLEDGMENTS

This work was supported by the National Science Foundation through awards CHE-1125235 and CHE-1305427. We thank the Center for High performance Computing at the University of Utah for technical support and allocation of computer time.

REFERENCES

(1) Rosenfeld, D. *Science* **2000**, *287*, 1793−1796.
(2) Zhang, R.; Li, G.; Fan, J.; Wu, D. L.; Molina, M. J. *Proc. Natl. Acad. Sci. U.S.A.* **2007**, *104*, 5295−5299.
(3) Andreae, M. O.; Rosenfeld, D. *Earth-Sci. Rev.* **2008**, *89*, 13−41.
(4) Ebben, C. J.; Ault, A. P.; Ruppel, M. J.; Ryder, O. S.; Bertram, T. H.; Grassian, V. H.; Prather, K. A.; Geiger, F. M. *J. Phys. Chem. A* **2013**, *117*, 6589−6601.
(5) Monahan, E. C.; Fairall, C. W.; Davidson, K. L.; Boyle, P. J. *Q. J. R. Meteorol. Soc.* **2007**, *109*, 379−392.
(6) Tsigaridis, K.; Koch, D.; Menon, S. *J. Geophys. Res. D: Atmos.* **2013**, *118*, 220−235.
(7) Ault, A. P.; Guasco, T. L.; Ryder, O. S.; Baltrusaitis, J.; Cuadra-Rodriguez, L. A.; Collins, D. B.; Ruppel, M. J.; Bertram, T. H.; Prather, K. A.; Grassian, V. H. *J. Am. Chem. Soc.* **2013**, *135*, 14528−14531.
(8) Ault, A. P.; Moffet, R. C.; Baltrusaitis, J.; Collins, D. B.; Ruppel, M. J.; Cuadra-Rodriguez, L. A.; Zhao, D.; Guasco, T. L.; Ebben, C. J.; Geiger, F. M.; Bertram, T. H.; Prather, K. A.; Grassian, V. H. *Environ. Sci. Technol.* **2013**, *47*, 5603−5612.
(9) Prather, K. A.; Bertram, T. H.; Grassian, V. H.; Deane, G. B.; Stokes, M. D.; Demott, P. J.; Aluwihare, L. I.; Palenik, B. P.; Azam, F.; Seinfeld, J. H.; Moffet, R. C.; Molina, M. J.; Cappa, C. D.; Geiger, F. M.; Roberts, G. C.; Russell, L. M.; Ault, A. P.; Baltrusaitis, J.; Collins, D. B.; Corrigan, C. E.; Cuadra-Rodriguez, L. A.; Ebben, C. J.; Forestieri, S. D.; Guasco, T. L.; Hersey, S. P.; Kim, M. J.; Lambert, W. F.; Modini, R. L.; Mui, W.; Pedler, B. E.; Ruppel, M. J.; Ryder, O. S.; Schoepp, N. G.; Sullivan, R. C.; Zhao, D. *Proc. Natl. Acad. Sci. U.S.A.* **2013**, *110*, 7550−7555.
(10) Sun, L.; Li, X.; Hede, T.; Tu, Y.; Leck, C.; Agren, H. *J. Phys. Chem. B* **2012**, *116*, 3198−3204.
(11) Song, C. H.; Carmichael, G. R. *Atmos. Environ.* **1999**, *33*, 2203−2218.
(12) George, C.; Ponche, J. L.; Mirabel, P. *J. Phys. Chem.* **1994**, *98*, 8780−8784.
(13) Apodaca, R. L.; Huff, D. M. *Atmos. Chem. Phys.* **2008**, *8*, 7451−7463.
(14) Ravishankara, A. R. *Science* **1997**, *276*, 1058−1065.
(15) Abbatt, J. P. D.; Waschewsky, G. C. G. *J. Phys. Chem. A* **1998**, *102*, 3719−3725.
(16) Bogdan, A. *J. Phys. Chem. B* **2006**, *110*, 12205−12206.
(17) Bogdan, A. *J. Phys. Chem. A* **2010**, *114*, 10135−10139.
(18) Bogdan, A.; Molina, M. J. *J. Phys. Chem. A* **2010**, *114*, 2821−2829.
(19) Larson, B. H.; Swanson, B. D. *J. Phys. Chem. A* **2006**, *110*, 1907−1916.
(20) Swanson, B. D. *J. Atmos. Sci.* **2009**, *66*, 741−754.
(21) Talbot, R. W.; Dibb, J. E.; Loomis, M. B. *Geophys. Res. Lett.* **1998**, *25*, 1367−1370.
(22) Dibb, J. E. *Geophys. Res. Lett.* **1998**, *25*, 1375−1378.
(23) Bogdan, A.; Molina, M. J.; Tenhu, H.; Mayer, E.; Bertel, E.; Loerting, T. *J. Phys.: Condens. Matter* **2010**, *23*, 035103.
(24) Bogdan, A.; Loerting, T. *J. Phys. Chem. C* **2011**, *115*, 10682−10693.
(25) Murray, B. J.; Bertram, A. K. *Phys. Chem. Chem. Phys.* **2008**, *10*, 3287−3301.
(26) Angell, C. A.; Sare, E. J.; Donnella, J.; Macfarlane, D. R. *J. Phys. Chem.* **1981**, *85*, 1461−1464.
(27) Angell, C. A.; Sare, E. I. *J. Chem. Phys.* **1970**, *52*, 1058−1068.
(28) Koop, T.; Kapilashrami, A.; Molina, L. T.; Molina, M. J. *J. Geophys. Res.* **2000**, *105*, 26393−26402.
(29) Bogdan, A.; Molina, M. J.; Kulmala, M.; Tenhu, H.; Loerting, T. *Proc. Natl. Acad. Sci. U.S.A.* **2013**, *110*, E2439.
(30) Bogdan, A.; Molina, M. J.; Tenhu, H.; Mayer, E.; Loerting, T. *Nat. Chem.* **2010**, *2*, 197−201.
(31) Kulmala, M.; Vehkamäki, H.; Petäjä, T.; Dal Maso, M.; Lauri, A.; Kerminen, V. M.; Birmili, W.; McMurry, P. H. *J. Aerosol Sci.* **2004**, *35*, 143−176.
(32) McMurry, P. H. *Atmos. Environ.* **2000**, *34*, 1959−1999.
(33) Kulmala, M.; Kontkanen, J.; Junninen, H.; Lehtipalo, K.; Manninen, H. E.; Nieminen, T.; Petäjä, T.; Sipilä, M.; Schobesberger, S.; Rantala, P.; Franchin, A.; Jokinen, T.; Järvinen, E.; Äijälä, M.; Kangasluoma, J.; Hakala, J.; Aalto, P. P.; Paasonen, P.; Mikkilä, J.; Vanhanen, J.; Aalto, J.; Hakola, H.; Makkonen, U.; Ruuskanen, T.; Mauldin, R. L.; Duplissy, J.; Vehkamäki, H.; Bäck, J.; Kortelainen, A.; Riipinen, I.; Kurtén, T.; Johnston, M. V.; Smith, J. N.; Ehn, M.; Mentel, T. F.; Lehtinen, K. E. J.; Laaksonen, A.; Kerminen, V.-M.; Worsnop, D. R. *Science* **2013**, *339*, 943−946.
(34) Park, J. Y.; Lim, S.; Park, K. *J. Atmos. Ocean. Technol.* **2014**, *31*, 93−104.
(35) Blot, R.; Clarke, A. D.; Freitag, S.; Kapustin, V.; Howell, S. G.; Jensen, J. B.; Shank, L. M.; McNaughton, C. S.; Brekhovskikh, V. *Atmos. Chem. Phys.* **2013**, *13*, 7263−7278.
(36) Deshpande, C. G.; Pant, V.; Kamra, A. K. *Atmos. Res.* **2010**, *96*, 544−552.
(37) Pierce, J. R.; Adams, P. J. *J. Geophys. Res.* **2006**, *111*, D06203.
(38) Clarke, A. D.; Owens, S. R.; Zhou, J. *J. Geophys. Res.* **2006**, *111*, D06202.
(39) Mårtensson, E. M.; Nilsson, E. D.; de Leeuw, G.; Cohen, L. H.; Hansson, H. C. *J. Geophys. Res. D: Atmos.* **2003**, *108*, AAC15−11−AAC 15−12.
(40) Murphy, D. M.; Anderson, J. R.; Qulnn, P. K.; Mclnnes, L. M.; Brechtel, F. J.; Kreidenwels, S. M.; Middlebrook, A. M.; Pósfai, M.; Thomson, D. S.; Buseck, P. R. *Nature* **1998**, *392*, 62−65.
(41) Wyslouzil, B. E.; Wilemski, G.; Strey, R.; Heath, C. H.; Dieregsweiler, U. *Phys. Chem. Chem. Phys.* **2006**, *8*, 54−57.
(42) Pathak, H.; Wyslouzil, B.; Obeidat, A.; Wilemski, G. *Nucl. Atmos. Aerosols: 19th Int. Conf.* **2013**, *1527*, 472−475.
(43) Wilemski, G.; Obeidat, A.; Hrahsheh, F. *Nucl. Atmos. Aerosols: 19th Int. Conf.* **2013**, *1527*, 144−147.
(44) Chakraborty, P.; Zachariah, M. *J. Phys. Chem. A* **2007**, *111*, 5459−5464.
(45) Ma, X.; Chakraborty, P.; Henz, B. J.; Zachariah, M. R. *Phys. Chem. Chem. Phys.* **2011**, *13*, 9374−9384.
(46) Molinero, V.; Laria, D.; Kapral, R. *J. Chem. Phys.* **1998**, *109*, 6844−6853.
(47) Molinero, V.; Laria, D.; Kapral, R. *Phys. Rev. Lett.* **2000**, *84*, 455−458.
(48) Hou, G. L.; Lin, W.; Deng, S. H. M.; Zhang, J.; Zheng, W. J.; Paesani, F.; Wang, X. B. *J. Phys. Chem. Lett.* **2013**, *4*, 779−785.
(49) Husar, D. E.; Temelso, B.; Ashworth, A. L.; Shields, G. C. *J. Phys. Chem. A* **2012**, *116*, 5151−5163.
(50) Temelso, B.; Morrell, T. E.; Shields, R. M.; Allodi, M. A.; Wood, E. K.; Kirschner, K. N.; Castonguay, T. C.; Archer, K. A.; Shields, G. C. *J. Phys. Chem. A* **2012**, *116*, 2209−2224.
(51) Temelso, B.; Phan, T. N.; Shields, G. C. *J. Phys. Chem. A* **2012**, *116*, 9745−9758.
(52) Morreis, T. E.; Shields, G. C. *J. Phys. Chem. A* **2010**, *114*, 4266−4271.
(53) Diken, E. G.; Hammer, N. I.; Johnson, M. A.; Christie, R. A.; Jordan, K. D. *J. Chem. Phys.* **2005**, *123*, 164309.

(54) Kathmann, S.; Schenter, G.; Garrett, B. *J. Phys. Chem. C* **2007**, *111*, 4977−4983.
(55) Douady, J.; Calvo, F.; Spiegelman, F. *J. Chem. Phys.* **2008**, *129*, 154305.
(56) Lukyanov, S. I.; Zidi, Z. S.; Shevkunov, S. V. *J. Mol. Struct.: THEOCHEM* **2005**, *725*, 191−206.
(57) Lukyanov, S. I.; Zidi, Z. S.; Shevkunov, S. V. *Fluid Phase Equilib.* **2005**, *233*, 34−46.
(58) Zidi, Z. S. *J. Chem. Phys.* **2005**, *123*, 64309.
(59) Zidi, Z. S. *J. Chem. Phys.* **2012**, *137*, 124107.
(60) Vaida, V. *J. Chem. Phys.* **2011**, *135*, 020901.
(61) Ayala, R.; Martínez, J. M.; Pappalardo, R. R.; Marcos, E. S. *J. Chem. Phys.* **2004**, *121*, 7269−7275.
(62) Obrien, J. T.; Williams, E. R. *J. Am. Chem. Soc.* **2012**, *134*, 10228−10236.
(63) Perera, L.; Berkowitz, M. L. *J. Chem. Phys.* **1993**, *99*, 4222−4224.
(64) Perera, L.; Berkowitz, M. *J. Chem. Phys.* **1994**, *100*, 3085−3093.
(65) Couling, S. B.; Fletcher, J.; Horn, A. B.; Newnham, D. A.; McPheat, R. A.; Williams, R. G. *Phys. Chem. Chem. Phys.* **2003**, *5*, 4108−4113.
(66) Herb, J.; Xu, Y.; Yu, F.; Nadykto, A. B. *J. Phys. Chem. A* **2013**, *117*, 133−152.
(67) Shevkunov, S. V.; Lukyanov, S. I.; Leyssale, J. M.; Millot, C. *Chem. Phys.* **2005**, *310*, 97−107.
(68) Kelly, C. P.; Cramer, C. J.; Truhlar, D. G. *J. Phys. Chem. B* **2006**, *110*, 16066−16081.
(69) Kelly, C. P.; Cramer, C. J.; Truhlar, D. G. *J. Chem. Theory Comput.* **2005**, *1*, 1133−1152.
(70) Manka, A.; Pathak, H.; Tanimura, S.; Wölk, J.; Strey, R.; Wyslouzil, B. E. *Phys. Chem. Chem. Phys.* **2012**, *14*, 4505−4516.
(71) Bartell, L. S.; Chushak, Y. G. In *Water in Confining Geometries*; Buch, V., Devlin, J. P., Eds.; Springer-Verlag: Berlin Heidelberg, 2003.
(72) Huang, J.; Bartell, L. S. *J. Phys. Chem.* **1995**, *99*, 3924−3931.
(73) Johnston, J. C.; Molinero, V. *J. Am. Chem. Soc.* **2012**, *134*, 6650−6659.
(74) Li, T.; Donadio, D.; Galli, G. *Nat. Commun.* **2013**, *4*, 1887.
(75) Pan, D.; Liu, L.-M.; Slater, B.; Michaelides, A.; Wang, E. *ACS Nano* **2011**, *5*, 4562−4569.
(76) Han, Y. Y.; Shuai, J.; Lu, H. M.; Meng, X. K. *J. Phys. Chem. B* **2012**, *116*, 1651−1654.
(77) Molinero, V.; Moore, E. B. *J. Phys. Chem. B* **2009**, *113*, 4008−4016.
(78) Moore, E. B.; Molinero, V. *Nature* **2011**, *479*, 506−508.
(79) Moore, E. B.; Molinero, V. *Phys. Chem. Chem. Phys.* **2011**, *13*, 20008−20016.
(80) Moore, E. B.; Allen, J. T.; Molinero, V. *J. Phys. Chem. C* **2012**, *116*, 7507−7514.
(81) Moore, E. B.; Molinero, V. *J. Chem. Phys.* **2009**, *130*, 244505−244512.
(82) Moore, E. B.; de la Llave, E.; Welke, K.; Scherlis, D. A.; Molinero, V. *Phys. Chem. Chem. Phys.* **2010**, *12*, 4124−4134.
(83) González Solveyra, E.; De La Llave, E.; Scherlis, D. A.; Molinero, V. *J. Phys. Chem. B* **2011**, *115*, 14196−14204.
(84) Shepherd, T. D.; Koc, M. A.; Molinero, V. *J. Phys. Chem. C* **2012**, *116*, 12172−12180.
(85) Limmer, D. T.; Chandler, D. *J. Chem. Phys.* **2011**, *135*, 134503.
(86) Limmer, D. T.; Chandler, D. *J. Chem. Phys.* **2012**, *137*, 044509.
(87) Li, T.; Donadio, D.; Russo, G.; Galli, G. *Phys. Chem. Chem. Phys.* **2011**, *13*, 19807−19813.
(88) Bullock, G.; Molinero, V. *Faraday Discuss.* **2013**, *167*, 371−388.
(89) Lupi, L.; Hudait, A.; Molinero, V. *J. Am. Chem. Soc.* **2014**, *136*, 3156−3164.
(90) Lupi, L.; Molinero, V. *J. Phys. Chem. A* **2014**, DOI: 10.1021/jp4118375.
(91) Kastelowitz, N.; Johnston, J. C.; Molinero, V. *J. Chem. Phys.* **2010**, *132*, 124511.
(92) Le, L.; Molinero, V. *J. Phys. Chem. A* **2011**, *115*, 5900−5907.
(93) Plimpton, S. *J. Comput. Phys.* **1995**, *117*, 1−19.
(94) Steinhardt, P. J.; Nelson, D. R.; Ronchetti, M. *Phys. Rev. B* **1983**, *28*, 784−805.
(95) Baron, R.; Molinero, V. *J. Chem. Theory Comput.* **2012**, *8*, 3696−3704.
(96) Vega, C.; de Miguel, E. *J. Chem. Phys.* **2007**, *126*, 154707.
(97) Stillinger, F. H.; Weber, T. A. *Phys. Rev. B* **1985**, *31*, 5262−5271.
(98) Angell, C. A. *J. Chem. Phys.* **1968**, *49*, 4713−4714.
(99) Kanno, H. *J. Phys. Chem.* **1987**, *91*, 1967−1971.
(100) Suzuki, Y.; Mishima, O. *Phys. Rev. Lett.* **2000**, *85*, 1322−1325.
(101) Moore, E. B.; Molinero, V. *J. Chem. Phys.* **2010**, *132*, 244504−244510.
(102) Jungwirth, P.; Tobias, D. J. *Chem. Rev.* **2006**, *106*, 1259−1281.
(103) Koop, T.; Luo, B.; Tsias, A.; Peter, T. *Nature* **2000**, *406*, 611−614.
(104) Knopf, D. A.; Lopez, M. D. *Phys. Chem. Chem. Phys.* **2009**, *11*, 8056−8068.
(105) Knopf, D. A.; Forrester, S. M. *J. Phys. Chem. A* **2011**, *115*, 5579−5591.
(106) Kumar, A. *J. Phys. Chem. B* **2007**, *111*, 10985−10991.
(107) Gerding, M.; Höffner, J.; Lautenbach, J.; Rauthe, M.; Lübken, F. J. *Atmos. Chem. Phys.* **2008**, *8*, 7465−7482.
(108) Hock, C.; Schmidt, M.; Kuhnen, R.; Bartels, C.; Ma, L.; Haberland, H.; VIssendorff, B. *Phys. Rev. Lett.* **2009**, *103*, 073401.
(109) Bartell, L.; Huang, J. *J. Phys. Chem.* **1994**, *98*, 7455−7457.
(110) Toxvaerd, S.; Larsen, N.; Dyre, J. C. *J. Phys. Chem. C* **2011**, *115*, 12808−12814.
(111) Bove, L. E.; Dreyfus, C.; Torre, R.; Pick, R. M. *J. Chem. Phys.* **2013**, *139*, 044501.
(112) Brukhno, A. V.; Anwar, J.; Davidchack, R.; Handel, R. *J. Phys.: Condens. Matter* **2008**, 20.
(113) Hansen, T. C.; Koza, M. M.; Kuhs, W. F. *J. Phys.: Condens. Matter* **2008**, 20.
(114) Moore, E. B.; Molinero, V. *Phys. Chem. Chem. Phys.* **2011**, *13*, 20008−20016.
(115) Morishige, K.; Uematsu, H. *J. Chem. Phys.* **2005**, *122*, 44711.
(116) Kuhs, W. F.; Sippel, C.; Falenty, A.; Hansen, T. C. *Proc. Natl. Acad. Sci. U. S. A.* **2012**, *109*, 21259−21264.
(117) Malkin, T. L.; Murray, B. J.; Brukhno, A. V.; Anwar, J.; Salzmann, C. G. *Proc. Natl. Acad. Sci. U. S. A.* **2012**, *109*, 1041−1045.
(118) Murray, B. J.; Knopf, D. A.; Bertram, A. K. *Nature* **2005**, *434*, 202−205.
(119) Elarby-Aouizerat, A.; Jal, J.-F.; Chieux, P.; Letoffé, J. M.; Claudy, P.; Dupuy, J. *J. Non-Cryst. Solids* **1988**, *104*, 203−210.
(120) Elarby-Aouizerat, A.; Jal, J.-F.; Dupuy, J.; Schildberg, H.; Chieux, P. *J. Phys. (Paris), Colloque* **1987**, *48*, 465−470.
(121) Breslow, R.; Guo, T. *Proc. Natl. Acad. Sci. U.S.A.* **1990**, *87*, 167−169.
(122) Sun, L.; Hede, T.; Tu, Y.; Leck, C.; Agren, H. *J. Phys. Chem. A* **2013**, *117*, 10746−10752.
(123) Tolman, R. C. *J. Chem. Phys.* **1949**, *17*, 333.
(124) Tolman, R. C. *J. Chem. Phys.* **1949**, *17*, 118.
(125) Joswiak, M. N.; Duff, N.; Doherty, M. F.; Peters, B. *J. Phys. Chem. Lett.* **2013**, *4*, 4267−4272.
(126) Factorovich, M. H.; Molinero, V.; Scherlis, D. A. *J. Am. Chem. Soc.* **2014**, *136*, 4508−4514.
(127) Koga, K.; Zeng, X. C.; Shchekin, A. K. *J. Chem. Phys.* **1998**, *109*, 4063−4070.
(128) Hardy, S. C.; Coriell, S. R. *J. Cryst. Growth* **1973**, *20*, 292−300.
(129) Ketcham, W. M.; Hobbs, P. V. *Philos. Magn.* **1969**, *19*, 1161−1173.
(130) Wood, G. R.; Walton, A. G. *J. Appl. Phys.* **1970**, *41*, 3027−3036.
(131) Rasmussen, D.; MacKenzie, A. In *Water Structure at the Water−Polymer Interface*; Jellinek, H. H. G., Ed.; Springer: New York, 1972; pp 126−145.
(132) Bogdan, A. *J. Chem. Phys.* **1997**, *106*, 1921−1929.
(133) Knight, C. A. *Philos. Magn.* **1971**, *23*, 153−165.
(134) Bogdan, A.; Molina, M. J.; Kulmala, M.; Tenhu, H.; Loerting, T. *Proc. Natl. Acad. Sci. U.S.A.* **2014**, *110*, E2439.

(135) Weissenborn, P. K.; Pugh, R. J. *J. Colloid Interface Sci.* **1996**, *184*, 550−563.
(136) Johnston, J. C.; Spencer, J.; Molinero, V. *manuscript in preparation*.
(137) Hribar, B.; Southall, N.; Vlachy, V.; Dill, K. *J. Am. Chem. Soc.* **2002**, *124*, 12302−12311.
(138) Martin, S. T. *Chem. Rev.* **2000**, *100*, 3403−3454.
(139) Monnin, C.; Dubois, M.; Papaiconomou, N.; Simonin, J.-P. *J. Chem. Eng. Data* **2002**, *47*, 1331−1336.
(140) Reguera, D.; Reiss, H. *J. Chem. Phys.* **2003**, *119*, 1533−1546.
(141) Němec, T. s.; Maršík, F. e.; Palmer, D. A. *J. Chem. Phys.* **2006**, *124*, 044509.
(142) Kuhs, W. F.; Sippel, C.; Falenty, A.; Hansen, T. C. *Proc. Natl. Acad. Sci. U.S.A.* **2013**, *110*, E2440.
(143) Jin, R.; Chu, L. T. *J. Phys. Chem. A* **2007**, *111*, 7833−7840.
(144) Jin, R.; Chu, L. T. *J. Phys. Chem. A* **2006**, *110*, 8719−8728.
(145) Jin, R.; Chu, L. T. *J. Phys. Chem. A* **2006**, *110*, 3647−3654.
(146) Fernandez, M. A.; Hynes, R. G.; Cox, R. A. *J. Phys. Chem. A* **2005**, *109*, 9986−9996.